Journal of the Mechanical Behavior of Biomedical Materials 184 (2026) 107648



Contents lists available at ScienceDirect

Journal of the Mechanical Behavior of Biomedical Materials

journal homepage: www.elsevier.com/locate/jmbbm





# Gradient orientation governs mechanical and regenerative outcomes in functionally graded bone scaffolds: a coupled finite element–agent-based modelling study

Ali Entezari [a,b,d,*,1], Vahid Badali [b,c,1], Georg N. Duda [b], Sara Checa [b,d,**]

[a] School of Biomedical Engineering, Faculty of Engineering and Information Technology, University of Technology Sydney, Sydney, NSW, 2007, Australia
[b] Julius Wolff Institute, Berlin Institute of Health, Charité—Universitätsmedizin Berlin, Berlin, Germany
[c] Department of Structural Mechanics and Analysis, Technische Universität Berlin, Berlin, Germany
[d] Institute of Biomechanics, Hamburg University of Technology (TUHH), Hamburg, Germany

ARTICLE INFO

*Keywords:*
Functionally graded scaffolds
Bone regeneration
Tissue engineering
Scaffold biomechanics
Computational modelling

ABSTRACT

Critical-sized bone defects remain a major clinical challenge, requiring scaffolds that combine mechanical stability with regenerative capacity. Functionally graded scaffolds offer a promising strategy by spatially varying porosity to optimise load transfer and tissue ingrowth. Here, we apply an established coupled poroelastic finite element–agent-based modelling (FEA–ABM) framework as a comparative platform to evaluate six cylindrical scaffold configurations modelled using Ti–6Al–4V material properties: two opposing axial-gradient designs, two opposing radial-gradient designs, and their corresponding uniform controls under physiologically representative loading. Poroelastic finite element analysis was used to compute local shear strain and fluid velocity, which regulated progenitor differentiation, proliferation, apoptosis, and migration in the agent-based model. Simulations representing 150 days of healing showed that axial gradients with larger pores at the host bone interface produced the greatest bone ingrowth, reaching approximately 77% pore occupancy compared with 69% in the uniform axial scaffold and 60% in the opposite axial gradient. In contrast, radial gradients did not substantially alter overall bone regeneration compared with the uniform radial scaffold, but the design with denser peripheral struts markedly improved mechanical performance, reducing volume-weighted P99 von Mises stress to approximately 41 MPa compared with about 57-71 MPa in the radial uniform and opposite radial-gradient designs. These findings reveal a design trade-off between regenerative capacity and structural competence, suggesting that gradient orientation should be selected according to the mechanical and biological requirements of the target defect environment. By applying the FEA–ABM framework consistently across the investigated configurations, this study provides comparative evidence to inform the selection of pore-size-gradient designs according to the regenerative and mechanical requirements of the target defect.

## 1. Introduction

Treatment of bone defects resulting from trauma, tumour resection, or degenerative disease remains a major challenge in orthopaedic surgery (Lee et al., 2022). Current clinical options for reconstruction primarily rely on autografts and allografts, but both approaches present serious limitations such as limited availability, donor-site morbidity, risk of immune rejection, and disease transmission (Fillingham and Jacobs, 2016; Ho-Shui-Ling et al., 2018). A promising alternative is bone tissue engineering, which seeks to regenerate bone by combining biological factors with engineered constructs (Bose et al., 2012). Central to this approach are porous three-dimensional scaffolds, typically fabricated from biocompatible and osteoconductive materials, which not only provide mechanical stability but also act as a substrate to guide cellular infiltration, vascularisation, and new bone formation within the defect site (Roseti et al., 2017).

* Corresponding author. School of Biomedical Engineering, Faculty of Engineering and Information Technology, University of Technology Sydney, Sydney, NSW, 2007, Australia.
** Corresponding author. Institute of Biomechanics, Hamburg University of Technology (TUHH), Hamburg, Germany.
*E-mail addresses:* ali.entezari@uts.edu.au (A. Entezari), sara.checa@tuhh.de (S. Checa).
[1] Ali Entezari and Vahid Badali contributed equally to this work.

https://doi.org/10.1016/j.jmbbm.2026.107648
Received 1 July 2026; Received in revised form 13 August 2026; Accepted 22 September 2026
Available online 23 September 2026
1751-6161/© 2026 The Authors. Published by Elsevier Ltd. This is an open access article under the CC BY license (http://creativecommons.org/licenses/by/4.0/).

Despite considerable progress in bone tissue engineering over recent decades, the treatment of critical-sized defects remains far from optimal (Xu et al., 2024a). A central challenge lies in achieving the right balance between mechanical strength and regenerative capacity (Roseti et al., 2017). Scaffolds must not only provide sufficient stability to withstand physiological loads in weight-bearing sites, but also facilitate effective bone regeneration (Entezari et al., 2020a). To address this dual requirement, functionally graded (FG) scaffolds have emerged as a promising strategy (Xiong et al., 2020). These scaffolds are inspired by natural bone, which displays gradual architectural transitions across regions of differing density and porosity. Mimicking such gradients, numerical studies have recently explored FG scaffold architectures to improve their biomechanical properties (Distefano et al., 2025; Bora et al., 2023; Kong et al., 2023).

Recent studies support FG scaffold designs as a means to reconcile mechanical competence with osteogenesis (Dubey et al., 2022). Pore-size gradients, implemented axially or radially, have been shown to tune stiffness, stress distribution, and fluid transport properties, thereby improving cell attachment and overall regenerative potential compared with uniform architectures (Mukasheva et al., 2024). For example, Xu et al. demonstrated that gradient pore-change strategies in triply periodic minimal surface scaffolds fabricated via selective laser sintering result in distinct mechanical responses and fluid-flow characteristics (Xu et al., 2024b). Similarly, Di Luca et al. showed that introducing pore-size gradients enhances the osteogenic differentiation of human mesenchymal stromal cells, highlighting the biological relevance of graded architectures for bone regeneration (Di Luca et al., 2016). More recently, Xiao et al. reported that gradient Schwarz Primitive scaffolds with thin-board integration achieved improved mechanical stability and promoted osteoblast adhesion and proliferation, further underscoring the promise of graded architectures for clinical translation (Xiao et al., 2025). While these studies have provided valuable insights into the role of FG scaffolds in osteogenesis, most remain confined to in vitro settings and do not capture the complex mechano-biological environment of specific anatomical sites, which is critical for guiding scaffold optimisation.

Computational approaches have shown great potential as tools to evaluate the biomechanical properties of scaffolds and to optimise their design prior to experimental validation (Guo et al., 2026; Entezari et al., 2020b). Finite element analysis (FEA) has been widely employed to predict stress distribution, effective stiffness, load transfer, and permeability in porous structures, while mechanobiological models have been used to simulate scaffold-guided bone regeneration (Gryko et al., 2022; Entezari et al., 2023; Asbai-Ghoudan et al., 2023;Yan et al., 2022). By integrating these methods, it becomes possible to systematically explore scaffold architectures and identify optimal designs that balance mechanical competence with biological performance (Wu et al., 2021). For example, Rezapourian and Hussainova recently performed a finite element study on hydroxyapatite-based Voronoi scaffolds with graded design parameters, showing that applying gradients in pore seed spacing and strut thickness improved load-bearing capacity and resulted in more favourable stress distribution compared to uniform scaffolds, highlighting the potential of irregular graded lattices to better mimic the structure and function of bone (Rezapourian and Hussainova, 2023). More recently, Wu et al. introduced a data–driven dynamic optimisation framework to design functionally graded ceramic scaffolds with vertical and lateral porosity gradients, reporting that both gradient strategies enhanced long-term bone regeneration compared to uniform designs, with lateral gradients producing the most pronounced improvements (Wu et al., 2024a). Collectively, these studies establish that graded porosity can influence scaffold mechanics and predicted bone regeneration. The question addressed in the present study is therefore narrower: how pore-size-gradient orientation and direction affect regenerative and mechanical outcomes when opposing axial and radial configurations are evaluated.

Previous computational investigations of scaffold-guided bone regeneration have commonly employed continuum mechanoregulation, tissue-differentiation, or remodelling formulations, in which local tissue formation or material properties are updated according to mechanical stimuli (Asbai-Ghoudan et al., 2023; Wu et al., 2021). Although these approaches can capture mechanically driven tissue evolution, they generally do not explicitly represent spatially discrete cellular activities such as migration, proliferation, differentiation, and apoptosis. Agent-based models (ABM) can explicitly represent these processes while retaining regulation by mechanical stimuli calculated through finite element analysis (Perier-Metz et al., 2020, 2022a; Badali et al., 2024; Dazzi et al., 2025). For example, Perier-Metz et al. coupled an ABM with finite element analysis to simulate progenitor cell migration, proliferation, differentiation, and apoptosis within large bone defects, allowing prediction of how scaffold design parameters influence bone regeneration outcomes (Perier-Metz et al., 2022b). Similarly, Jaber et al. applied a hybrid ABM–FEA framework to capture mesenchymal cell migration, osteoblast proliferation and differentiation, and fibroblast activity within scaffold pores, enabling comparison of regeneration dynamics between gyroid and strut-like architectures in a large femoral defect (Jaber et al., 2022). Although coupled ABM–FEA models have previously been applied to scaffold-supported bone regeneration, to the best of our knowledge, they have not been used to systematically evaluate pore-size-graded scaffolds. In particular, the regenerative and mechanical effects of opposing axial and radial gradient directions, relative to corresponding uniform scaffolds, have not been compared within a common model under physiologically representative loading.

In this study, we use an established coupled FEA–ABM framework (Perier-Metz et al., 2020) as a comparative computational platform to investigate six scaffold configurations: two opposing axial-gradient designs and a corresponding uniform control, together with two opposing radial-gradient designs and a corresponding uniform control. Within each orientation group, the scaffolds had approximately equivalent overall porosity. The objectives were to determine how gradient orientation and direction influenced (i) the spatial and temporal progression of predicted bone regeneration and (ii) the spatial distribution and magnitude of scaffold stress under physiologically representative loading.

## 2. Materials and methods

### 2.1. Scaffold designs

Scaffolds with either radial or axial pore-size gradients were generated to investigate the influence of graded architectures on both mechanical performance and tissue regeneration. All scaffold models were designed as cylinders with a diameter of 21 mm and a height of 30 mm, matching the dimensions of the defect region in the sheep tibia.

For the axial gradients (Fig. 1), two types were created. In Type 1 (AGS-1), pore size increased from the top and bottom surfaces toward the central region, providing larger pores in the scaffold core while maintaining tighter pore networks at the host–scaffold interfaces. In Type 2 (AGS-2), pore size decreased toward the central region, representing an exploratory design in which the effect of a denser mid-height on mechanical stability could be evaluated. An axial uniform scaffold (AUS) with constant pore size was also included as a reference. To ensure comparability, all three scaffolds in this category were generated with an overall porosity of approximately 45%, allowing the effects of pore-size gradients to be isolated from changes in bulk porosity. The uniform scaffold had a pore size of 1.6 mm, while the largest and smallest pore sizes in the gradient scaffolds were 2.55 and 0.65 mm, respectively. Increasing the overall porosity beyond this level would require further enlargement of the upper pore-size range, which may reduce available surface area for bone bridging and has been reported to be less favourable for bone formation when pores become excessively large (Entezari et al., 2024).

For the radial gradients (Fig. 2), two types were created. In Type 1

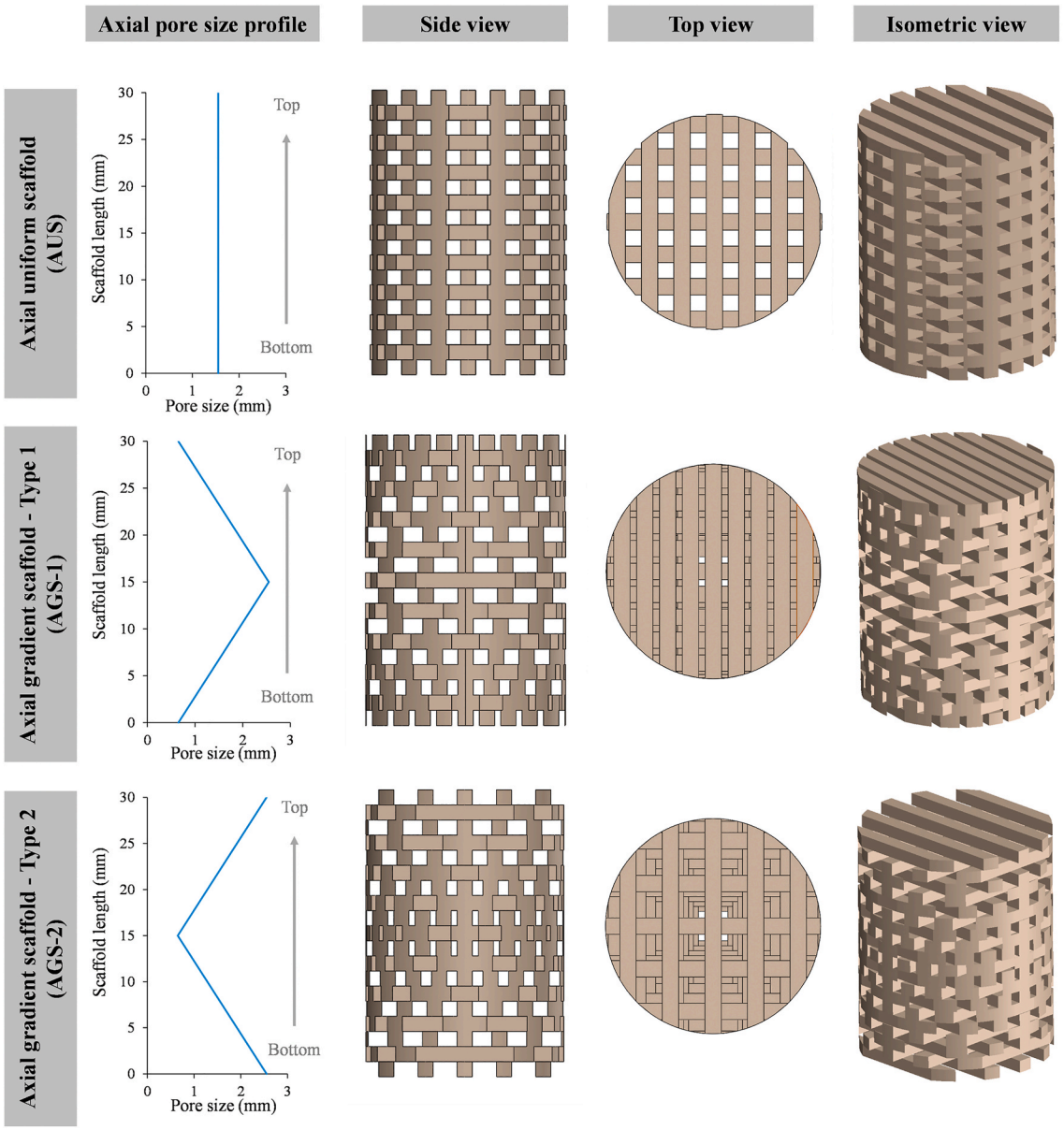



**Fig. 1. Scaffold designs with different axial pore-size distributions.** The first row shows an axial uniform scaffold (AUS) with constant pore size. The second row presents an axial gradient scaffold Type 1 (AGS-1), where pore size increases from the top and bottom surfaces toward the central region. The third row illustrates an axial gradient scaffold Type 2 (AGS-2), where pore size decreases from the surfaces toward the central region. For each scaffold type, the pore-size profile, side view, top view, and isometric view are provided to demonstrate architectural variations.

(RGS-1), pore size gradually decreased from the centre toward the periphery, whereas in Type 2 (RGS-2) it decreased from the periphery toward the centre. The RGS-1 design, with denser struts at the periphery, draws inspiration from the femoral architecture, where a stiff cortical shell surrounds a more porous trabecular core. A radial uniform scaffold (RUS) with a constant pore size served as the control. As with the axial gradients, all three scaffolds in this category were designed with an overall porosity of approximately 45%. The uniform scaffold had a pore size of 1.5 mm. In RGS-1, the largest and smallest pore sizes were 1.85 and 0.50 mm, respectively, whereas in RGS-2 they were 2.05 and 0.55 mm. Notably, unlike the axial gradients, where AGS-1 and AGS-2 exhibited similar maximum and minimum pore sizes, the radial gradient scaffolds required different pore sizes between RGS-1 and RGS-2 in order to maintain porosity consistency. The lower bound was set by biological considerations, as experimental studies indicate that pore sizes of at least ~300 μm are required to support adequate vascularisation and nutrient supply (De Witte et al., 2018; Entezari et al., 2019).

### 2.2. Integration of finite element and agent-based models

The poroelastic FE formulation, ABM cell-activity rules, mechanoregulation algorithm, and iterative coupling procedure were adapted from the framework reported in our previous study (Perier-Metz et al., 2020). In the present study, this established framework was applied consistently across the six scaffold configurations to evaluate the influence of gradient orientation and direction. The following subsections summarise the framework for completeness and describe its application to the scaffold designs investigated here.

In the previous study (Perier-Metz et al., 2020), model predictions were evaluated against radiographs acquired at four-week intervals and histological images and histomorphometric bone-area measurements obtained at 24 weeks from a plate-stabilised 4-cm tibial defect in sheep containing an autograft-filled, 3D printed titanium honeycomb scaffold. The present implementation used closely comparable idealised cortical-bone dimensions, a broadly comparable unilateral steel plate

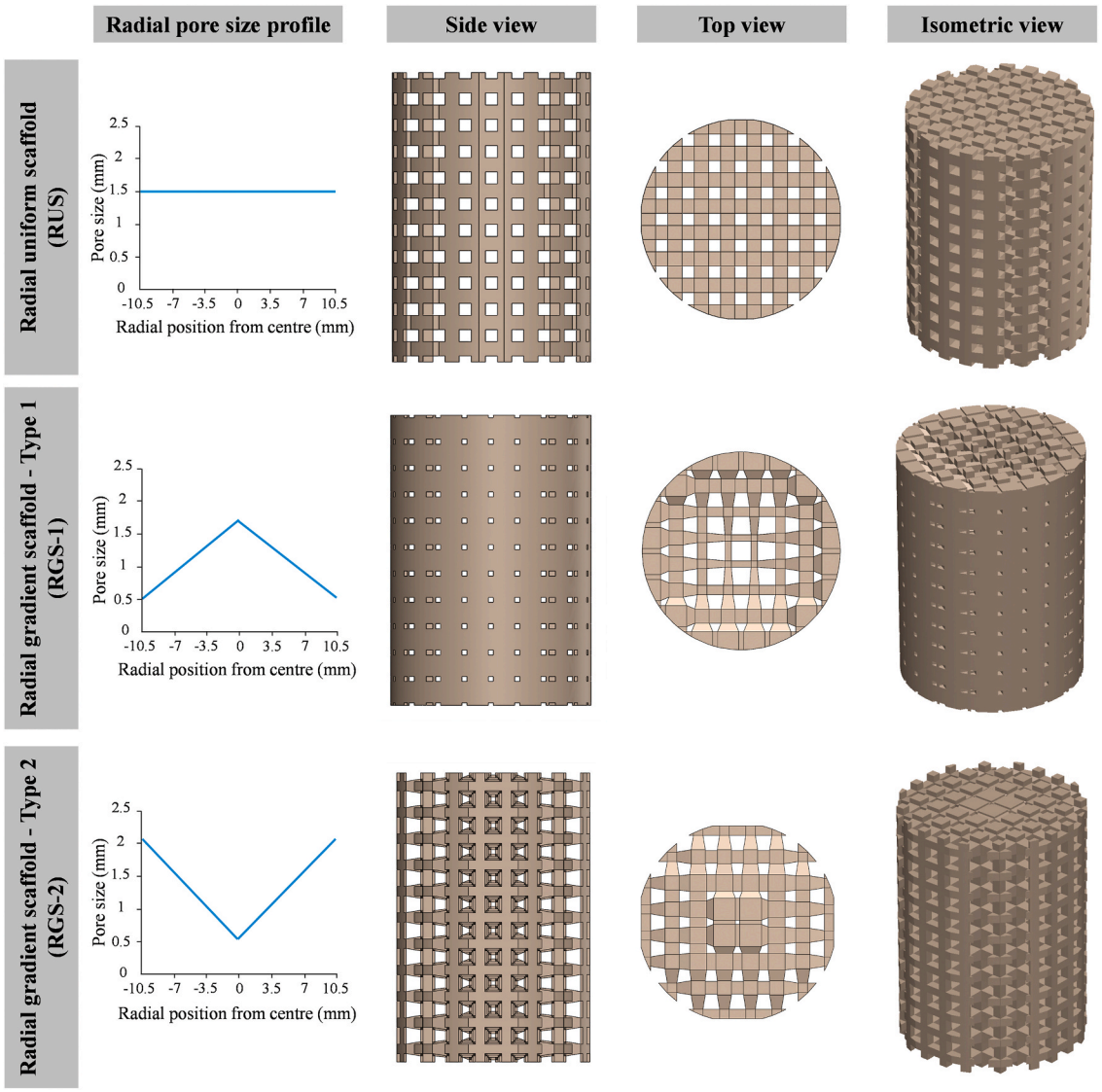



**Fig. 2. Scaffold designs with different radial pore-size distributions.** The first row shows a radial uniform scaffold (RUS) with constant pore size. The second row illustrates a radial gradient scaffold Type 1 (RGS-1), where pore size gradually increases from the periphery toward the centre. The third row depicts a radial gradient scaffold Type 2 (RGS-2), where pore size decreases from the periphery toward the centre. For each scaffold type, the pore-size profile, side view, top view, and isometric view are presented to highlight the architectural differences.

fixation arrangement, the same axial load and bending moment, and the same reported poroelastic properties for tissue types common to both models, mechanoregulation thresholds, and cell-activity rates. However, it differed from the model reported in (Perier-Metz et al., 2020) in terms of defect length, scaffold architecture, and the absence of autograft and its associated osteoconductive effects. The previous study therefore provides experimental evaluation of selected aspects of the underlying modelling approach but does not constitute direct validation of the six scaffold configurations investigated here. Accordingly, the present model was used for controlled comparative analysis rather than case-specific quantitative prediction.

### 2.2.1. *Finite element model*

In the present study, a poroelastic finite element (FE) model (Perier-Metz et al., 2020) was implemented to characterise the mechanical environment within a large bone defect stabilised by a fixation plate and containing the scaffold (Fig. 3a). A generic locking-plate fixation was represented using an idealised plate–screw assembly (not corresponding to a specific commercial design). Plate and screw dimensions and material properties were held constant across all cases so that observed differences arose from scaffold architecture. Scaffold geometries were generated in SolidWorks (Dassault Systèmes, France) and imported into Abaqus/CAE (Dassault Systèmes, Providence, RI, USA), where they were positioned within an idealised cylindrical defect domain. The cortical bone, representing sheep tibial geometry, was modelled as a hollow cylinder with an outer diameter of 21 mm and an inner diameter of 15 mm. A callus domain was defined to surround the scaffold externally and to infiltrate the pore space within the scaffold, thereby enabling tissue deposition both around and inside the construct.

Biological tissues were represented as poroelastic materials with distinct elastic, permeability, and bulk modulus properties (Table 1), allowing the simultaneous consideration of solid and fluid phases throughout the healing environment (Perier-Metz et al., 2020, 2022a). In contrast, the implant components were modelled as linear elastic solids: the scaffold was assigned the properties of Ti-6Al-4V alloy (Young's modulus 104 GPa, Poisson's ratio 0.3), and the fixation plate and screws were assigned the properties of 316 L stainless steel (Young's modulus 200 GPa, Poisson's ratio 0.305) (Pobloth et al., 2018). The cortical-bone and callus domains were discretised using 10-node modified tetrahedral pore-pressure elements (C3D10MP) to represent

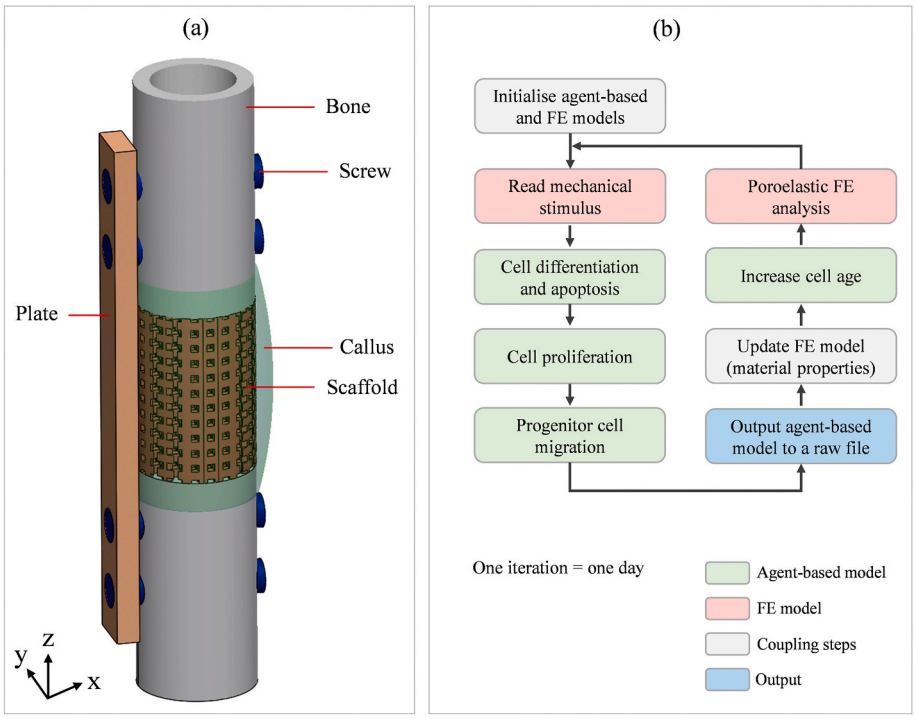



**Fig. 3. Integration of finite element (FE) and agent-based modelling for scaffold-guided bone regeneration.** (a) Schematic of a scaffold implanted within a bone defect stabilised by a fixation plate. (b) Coupled computational workflow: mechanical stimuli are obtained from poroelastic FE analysis and transferred to the agent-based model, where cell differentiation, apoptosis, proliferation, and progenitor migration are simulated. The updated cell distribution alters local tissue material properties, which are fed back into the FE model in an iterative loop until regeneration outcomes are predicted.

**Table 1**
Material properties assigned to tissues.

| Property | Callus (granulation) | Fibrous tissue | Cartilage | Immature bone | Mature bone | Cortical bone |
|---|---|---|---|---|---|---|
| **Young's modulus (MPa)** | 0.2 | 2 | 10 | 1000 | 17,000 | 17,000 |
| **Permeability ($10^{-14}$ $m^4$/Ns)** | 1 | 1 | 0.5 | 10 | 37 | 0.001 |
| **Poisson's ratio** | 0.167 | 0.167 | 0.3 | 0.3 | 0.3 | 0.3 |
| **Bulk modulus of grains (MPa)** | 2300 | 2300 | 3700 | 13,940 | 13,940 | 13,920 |
| **Bulk modulus of fluid (MPa)** | 2300 | 2300 | 2300 | 2300 | 2300 | 2300 |

their coupled poroelastic response. The scaffold was discretised using 10-node quadratic tetrahedral elements (C3D10), whereas the fixation plate and screws were discretised using four-node linear tetrahedral elements (C3D4).

Physiological loading representative of sheep gait was applied. Specifically, an axial compressive load of 1372 N, corresponding to approximately two times the body weight of a sheep, together with a bending moment of 17.125 Nm was imposed on the proximal bone extremity (Duda et al., 1997), while the distal end was fully constrained in both translation and rotation. The FE analysis, performed in Abaqus/-Standard, provided spatial distributions of interstitial fluid velocity and octahedral shear strain, which were subsequently transferred to the agent-based model to regulate cell activity and tissue differentiation.

Quantitative scaffold-stress comparisons were based on the volume-weighted 99th-percentile (P99) von Mises stress, calculated from integration-point stress values using integration-point volume as the weighting factor. Mesh convergence was assessed using RGS-1 because it contained the smallest scaffold struts and the smallest characteristic features within the callus domain among the six configurations, thereby representing the most demanding geometry for mesh resolution. Model selection was based on convergence of the scaffold P99 von Mises stress, while mesh independence within the callus was independently verified using the volume-weighted mean combined mechanobiological stimulus, $S$ (Equation (1)). Complete results for the scaffold and callus are provided in Tables S1 and S2, respectively, and representative finite element meshes are shown in Fig. S1 (Supplementary Material).

### 2.2.2. *Agent-based model*

We employed a previously established mechanobiological bone-regeneration model that has been evaluated against experimental observations of scaffold-guided bone healing (Perier-Metz et al., 2020, 2022a, 2022b). This model is a three-dimensional agent-based framework, implemented in C++ and coupled with the finite element model described in Section 2.2.1. Individual agents, each representing a 100 μm voxel, could correspond to a single cell phenotype, progenitor cell, fibroblast, chondrocyte, or immature/mature osteoblast, together with their respective extracellular matrix types: granulation tissue, fibrous tissue, cartilage, and immature or mature bone. At each daily time step, cells could proliferate, migrate, differentiate, or undergo apoptosis according to experimentally derived rates (Table 2) (Appeddu and Shur, 1994).

Cell differentiation was regulated by the local mechanical stimulus $S$, defined as a weighted combination of octahedral shear strain $\gamma$ and interstitial fluid velocity $v$ calculated in the FE model:

$$S = \frac{\gamma}{a} + \frac{v}{b} \tag{1}$$

where $a = 0.0375$ and $b = 0.003$ mm/s are scaling constants (Huiskes

**Table 2**
Cell activity parameters implemented in the agent-based model.

| Cell type | Proliferation rate ($day^{-1}$) | Apoptosis rate ($day^{-1}$) | Differentiation rate ($day^{-1}$) | Migration speed (μm/h) |
|---|---|---|---|---|
| **Progenitor cells** | 0.6 | 0.05 | 0.3 | 30 |
| **Fibroblasts** | 0.55 | 0.05 | – | – |
| **Chondrocytes** | 0.2 | 0.1 | – | – |
| **Osteoblasts** | 0.3 | 0.16 | – | – |

et al., 1997; Lacroix and Prendergast, 2002). The resulting values determined whether progenitor cells differentiated toward fibrous tissue, cartilage, immature bone, or mature bone, or underwent resorption under very low stimulus conditions (Table 3) (Perier-Metz et al., 2020). Differentiation events were linked to matrix deposition, thereby progressively altering the spatial distribution of tissue types within the callus and scaffold pores.

#### 2.2.3. Coupling strategy

The FE–ABM coupling (Fig. 3b) followed the two-way iterative workflow established in our previous study (Perier-Metz et al., 2020). At the start of each iteration, poroelastic FE analysis provided spatial maps of shear strain and fluid velocity under physiological loading. These values were imported into the ABM to guide cellular processes, including proliferation, migration, differentiation, and apoptosis. The updated tissue distribution modified the local mechanical properties, which were recalculated using a rule-of-mixtures approach and then passed back to the FE model. The new mechanical environment was resolved, and the cycle repeated. One iteration corresponded to one day of healing, allowing the coupled framework to capture the spatiotemporal evolution of scaffold-guided bone repair.

## 3. Results and discussion

Successful repair of critical-sized bone defects relies on scaffolds that can effectively guide and sustain bone regeneration within the defect site. Despite extensive progress in scaffold design, the influence of architectural gradients on the spatiotemporal progression of new tissue formation remains incompletely understood. To address this comparative design question, we applied the previously established FEA–ABM framework (Perier-Metz et al., 2020) to the six scaffold configurations under consistent geometrical, mechanical and biological conditions. Because the present construct does not correspond to a configuration-matched experimental model, the reported bone-occupancy and scaffold-stress values are interpreted as comparative predictions rather than case-specific quantitative estimates.

Fig. 4 illustrates the progression of regeneration within axial gradient scaffolds over 150 days at five representative time points, shown as cross-sections through the scaffold mid-plane. Simulations were run for 150 days, which is sufficient to capture the relative rate and spatial progression of bone ingrowth across designs; the objective was comparative assessment of scaffold performance rather than prediction of complete defect healing. Up to day 30, bone formation remained minimal across all designs, with MSCs predominantly occupying the peripheral scaffold regions near the host bone. By day 60, the first row of pores adjacent to the host bone, at both the proximal and distal ends, became populated with mature osteoblasts, marking the onset of bone deposition. As healing advanced, bone ingrowth progressed steadily from the defect boundaries toward the scaffold centre. By day 150, nearly the first three pore rows were completely filled with mature osteoblasts, while the fourth row contained a mixture of MSCs and newly differentiated bone cells. Although the overall temporal pattern of bone formation was consistent across the three scaffold types, quantitative differences were evident. AGS-2 scaffold, characterised by larger pores at the host bone interface, exhibited greater filling of the initial pore rows compared with both the AUS and AGS-1 designs, leading to a higher net volume of mature bone formation (Fig. 6).

**Table 3**
Mechano-regulation thresholds guiding progenitor cell differentiation.

| Stimulus range (S) | Tissue response |
|---|---|
| $S \leq 0.01$ | Bone resorption |
| $0.01 < S \leq 0.53$ | Mature bone |
| $0.53 < S \leq 1$ | Immature bone |
| $1 < S \leq 3$ | Cartilage |
| $S > 3$ | Fibrous tissue |

In contrast to the axial gradient designs, Fig. 5 highlights regeneration within radial gradient scaffolds, where pore-size gradients were oriented from the periphery toward the centre: Type 1 with larger central pores (RGS-1) and Type 2 with smaller central pores (RGS-2), alongside the radial uniform reference scaffold (RUS). The results are shown as cross-sections through the scaffold mid-plane.

During the early phase (day 30), bone formation was negligible, with MSCs concentrated along the cortical interface. By day 60, mature osteoblasts began to populate the outer pore layers, marking the onset of bone deposition from the periphery inward. From day 90 onward, bone ingrowth progressed toward the scaffold centre, though the depth of penetration varied between designs.

By day 150, both the RUS and RGS-1 scaffolds exhibited gradual inward progression, with bone formation more pronounced at the sides, reflecting the influence of peripheral deposition. In contrast, RGS-2 showed faster central ingrowth than the other two designs. Its smaller central pores likely offered greater surface area for cell attachment and bone growth, facilitating deeper infiltration toward the scaffold core (Deering et al., 2023). Despite these spatial differences, the total amount of bone formed remained broadly comparable across all three scaffold types (Fig. 6).

To complement the cross-sectional maps (Figs. 4 and 5), Fig. 6 reports quantitative bone ingrowth as a percentage of scaffold pore volume over time. In the axial gradient designs (Fig. 6a), all scaffolds showed a monotonic increase from ~3 to 4% at day 30 to 60–77% at day 150. Despite having similar overall porosity, Type 2 (AGS-2) yielded the highest occupancy at every time point, reaching approximately 21%, 39%, 59%, and 77% at days 60, 90, 120, and 150, respectively. At day 150, this corresponded to an approximately 12% higher bone occupancy than the uniform axial scaffold (AUS; ~69%) and 28% higher occupancy than Type 1 (AGS-1; ~60%). These trends are consistent with the cross-sectional observations: although the depth of ingrowth was comparable across designs, the larger pores positioned near the proximal and distal bone interfaces in AGS-2 facilitated greater overall bone deposition, whereas the smaller pores in AGS-1 limited net bone infill.

For the radial designs (Fig. 6b), ingrowth also increased steadily over time. However, differences in net bone formation were less pronounced, particularly between the radial uniform scaffold (RUS) and radial gradient scaffold Type 2 (RGS-2), which exhibited nearly identical values at later stages. Radial gradient scaffold Type 1 (RGS-1) performed comparably to the other two designs at early time points, but by day 150 its occupancy lagged slightly behind. Taken together, these results demonstrate that gradient scaffolds, and the orientation of the gradient (axial versus radial), can influence the amount of bone formation.

In addition to supporting bone regeneration, scaffolds must also provide sufficient mechanical stability to withstand physiological loading (Hollister, 2005). Accordingly, regenerative outcomes were considered together with the mechanical response of the scaffold. FEA was used to compare how the six scaffold architectures influenced the spatial distribution and volume-weighted P99 magnitude of von Mises stress under identical loading conditions.

Fig. 7 presents the von Mises stress maps for the uniform scaffold and the two axial gradient designs. Stresses were consistently higher on the

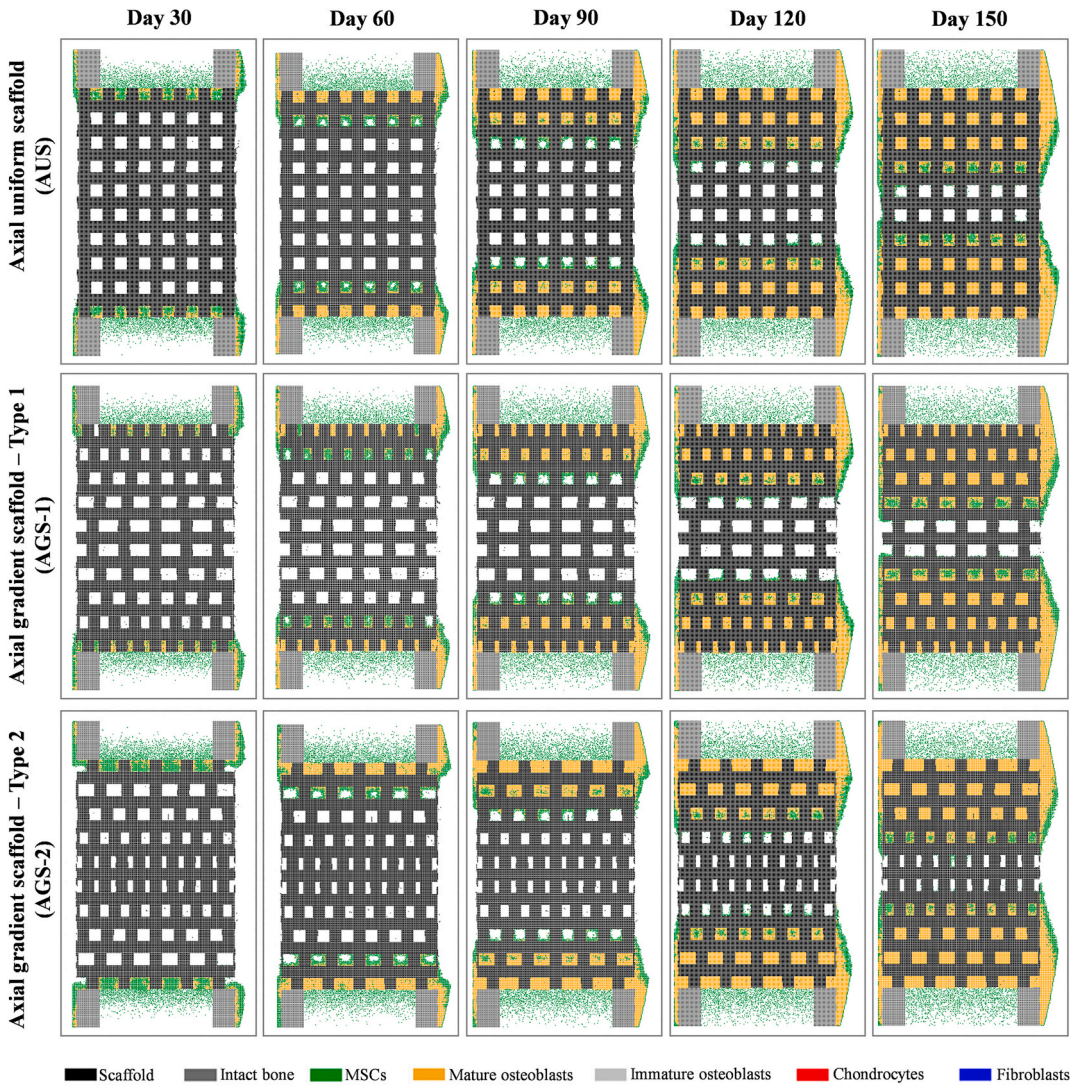



**Fig. 4. Temporal progression of tissue regeneration within axial gradient scaffolds, simulated using the coupled agent-based and finite element framework.** Each row corresponds to a different axial gradient scaffold type, and columns represent sequential time points during healing. The top row corresponds to the uniform scaffold (AUS), while the middle and bottom rows show axial gradient designs in which pore size increases (AGS-1) or decreases (AGS-2) toward the central region. The results illustrate how axial pore-size gradients influence spatial and temporal patterns of tissue ingrowth and remodelling. The results are shown as cross-sections through the scaffold mid-plane in the x–z plane. Colours are: scaffold (black), intact bone (dark grey), mesenchymal stromal cells—MSCs (green), mature osteoblasts (yellow), immature osteoblasts (light grey), chondrocytes (red), and fibroblasts (blue); white denotes unfilled pore/callus space. (For interpretation of the references to colour in this figure legend, the reader is referred to the Web version of this article.)

lateral side (opposite to the fixation plate). Moreover, elevated stresses were observed on the anterior side due to the applied bending moment. Stress concentrations were most pronounced at the anterior–lateral quadrant, localised around strut junctions, while the majority of struts experienced relatively low stresses.

Compared with the uniform design (AUS), the two gradient scaffolds redistributed stresses more heterogeneously along the scaffold height. AGS-2 exhibited elevated stresses near the proximal and distal ends, where pores were larger, whereas AGS-1 displayed higher stresses near the mid-height region, reflecting the larger pores present in this area. These spatial patterns demonstrate how pore-size gradients altered the internal stress distribution. This effect is expected to be particularly important when materials with lower mechanical properties, such as polymers or bioceramics, are used as scaffold materials (Brochu et al., 2024; Velasco et al., 2015). Overall, these findings indicate that axial pore-size gradients not only influence tissue regeneration but also play a significant role in governing mechanical load transfer through the scaffold.

Fig. 8 shows the von Mises stress distributions for the uniform scaffold and the two radial gradient designs. As in the axial case, stresses concentrated on the lateral side (opposite to the fixation plate) and the anterior side, consistent with the load path and bending moment.

Radial gradient direction influenced the peripheral scaffold stress distribution. RGS-1, with smaller pores and denser struts at the scaffold boundary, showed lower peripheral stress levels than the other radial configurations. In contrast, RGS-2, which had larger peripheral pores and thinner boundary struts, exhibited more localised regions of elevated peripheral stress, particularly in the anterior–lateral quadrant, while the uniform scaffold displayed an intermediate pattern. These trends are consistent with established mechanical principles: the denser peripheral struts of RGS-1 provided greater local load-bearing area, whereas the larger pores and thinner struts of RGS-2 reduced it. This relationship provides a mechanical basis for interpreting the configuration-dependent stress distributions observed across the radial designs.

Fig. 9 summarises the volume-weighted P99 von Mises stress for all

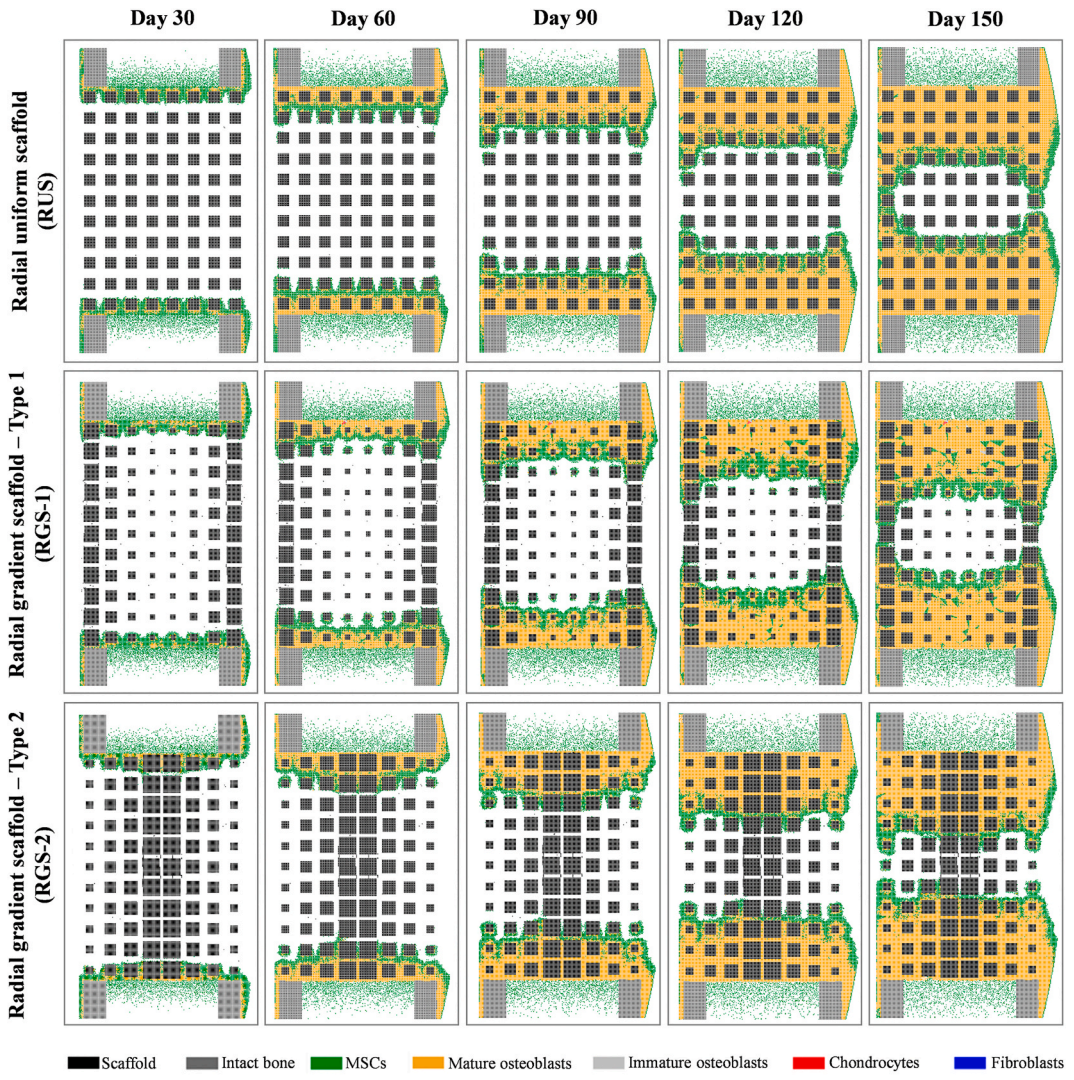



**Fig. 5. Temporal progression of tissue regeneration within radial gradient scaffolds, simulated using the coupled agent-based and finite element framework.** Each row corresponds to a different radial gradient scaffold type, and columns represent sequential time points during healing. The results illustrate how radial pore-size gradients influence spatial and temporal patterns of tissue ingrowth and remodelling. The results are shown as cross-sections through the scaffold mid-plane in the x–z plane. Colours are: scaffold (black), intact bone (dark grey), mesenchymal stromal cells—MSCs (green), mature osteoblasts (yellow-ochre), immature osteoblasts (light grey), chondrocytes (red), and fibroblasts (blue); white denotes unfilled pore/callus space. (For interpretation of the references to colour in this figure legend, the reader is referred to the Web version of this article.)

six scaffold configurations, complementing the spatial stress distributions shown in Figs. 7 and 8. This metric was used instead of the raw maximum stress to reduce sensitivity to isolated element-level stress concentrations and potential singularities at sharp geometric features. Among the axial configurations (Fig. 9a), both AGS-1 and AGS-2 exhibited higher P99 stress than AUS. AGS-2 had the highest value (86.2 MPa), followed by AGS-1 (71.6 MPa) and AUS (62.0 MPa). The higher P99 stress in AGS-2 was consistent with the elevated stresses observed near the proximal and distal ends, whereas the intermediate value for AGS-1 corresponded to higher stresses around its larger-pore mid-height region.

For the radial configurations (Fig. 9b), RGS-1 exhibited the lowest volume-weighted P99 von Mises stress (41.0 MPa), compared with 57.4 MPa for RUS and 71.4 MPa for RGS-2. This ordering is consistent with the greater local load-bearing area provided by the denser boundary struts of RGS-1. Conversely, the larger peripheral pores and thinner boundary struts of RGS-2 were associated with the highest P99 stress among the radial configurations.

Overall, axial gradients shifted regions of higher stress along the scaffold height and increased P99 stress relative to AUS, whereas radial gradient direction influenced both the peripheral stress distribution and P99 stress. When considered alongside the regenerative outcomes, these results indicate a configuration-dependent trade-off: AGS-2 produced greater predicted bone ingrowth when larger pores were positioned at the bone–scaffold interfaces, whereas RGS-1, with its denser peripheral ring, produced the lowest P99 scaffold stress. Within the investigated design space, these contrasting outcomes indicate that regenerative and mechanical performance should be considered jointly.

These patterns reflect the interplay between local pore architecture, load transfer, and cell–matrix interactions. In the axial designs, the larger pores positioned at the host-bone interfaces in AGS-2 may have provided additional space for cellular infiltration and matrix deposition, thereby facilitating greater net bone growth. By contrast, radial pore-size gradients did not provide a similar advantage for tissue ingrowth, consistent with recent in vivo findings showing that radially graded scaffolds did not outperform uniform controls in terms of bone formation (Deering et al., 2023). More broadly, the predicted tissue-growth and scaffold-stress trends are consistent with previous experimental and computational evidence that graded porosity can influence osteogenic responses, scaffold mechanics, and bone regeneration (Di Luca

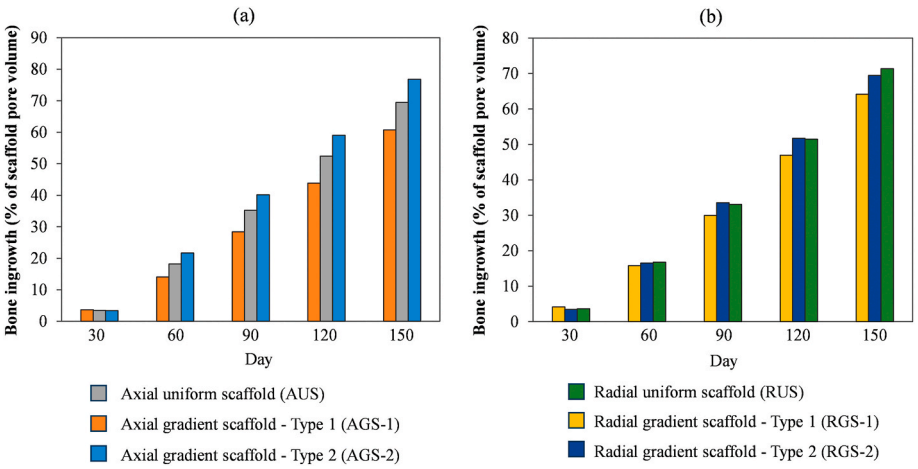



**Fig. 6. Quantitative evaluation of bone ingrowth within scaffolds over time.** (a) Comparison of bone ingrowth in axial uniform scaffold (AUS), axial gradient scaffold Type 1 (AGS-1), and axial gradient scaffold Type 2 (AGS-2). (b) Comparison of bone ingrowth in radial uniform scaffold, radial gradient scaffold Type 1 (RGS-1), and radial gradient scaffold Type 2 (RGS-2). Data are shown as the percentage of scaffold pore volume occupied by bone at sequential time points, illustrating how scaffold architecture influences bone ingrowth dynamics.

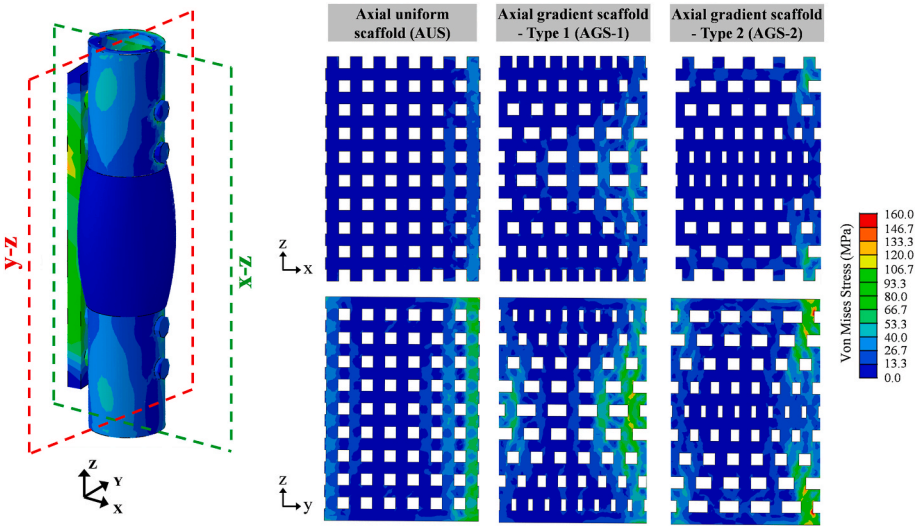



**Fig. 7. Von Mises stress distribution within axial uniform scaffold and axial gradient scaffolds (Type 1 and Type 2) under loading.** The top row shows the stress distribution across the mid-cross-section in the x–z plane, while the bottom row presents the distribution across the y–z plane, demonstrating the influence of scaffold architecture on stress distribution.

et al., 2016; Liu et al., 2025). Against this established background, evaluating opposing axial and radial gradients and their corresponding uniform controls under common mechanoregulation and loading conditions enabled the relative effects of gradient orientation and direction to be compared on a consistent basis.

Accordingly, the preferred gradient strategy may depend on the design priority and clinical context. For load-bearing defects such as long bones, designs with denser radial peripheries may warrant consideration when reducing scaffold stress is prioritised (Schulze et al., 2023). Conversely, axial gradients with larger pores at the host-bone interfaces may warrant investigation when promoting bone ingrowth is the primary objective. Selection of an appropriate architecture would also need to account for defect location, patient anatomy, and the local loading environment (Huo et al., 2021).

This study has several limitations. The present construct was deliberately idealised to enable a controlled comparison among scaffold configurations and did not reproduce a specific animal anatomy, commercial fixation system, or clinically implemented scaffold architecture. Although the underlying modelling approach was previously evaluated against serial radiographic and endpoint histological and histomorphometric observations from a plate-stabilised tibial defect in sheep (Perier-Metz et al., 2020), differences in defect length, scaffold topology, and biological conditions preclude direct validation of the present graded configurations using those data. Accordingly, the absolute bone-occupancy and scaffold-stress values should be interpreted as comparative model predictions rather than case-specific quantitative estimates, and the conclusions are restricted to relative differences among the six investigated configurations.

In addition, the scaffold was modelled using Ti–6Al–4V properties and therefore did not capture the time-dependent degradation and material-property evolution characteristic of biodegradable bioceramic or polymeric scaffolds (Chen et al., 2011). Consequently, the quantitative stress values and relative mechanical performance of the configurations should not be extrapolated directly to biodegradable scaffolds, whose different and evolving material properties may alter scaffold–tissue load sharing during degradation and regeneration. The cell-differentiation rules were derived from generalised mechanoregulation thresholds rather than subject-specific data, and

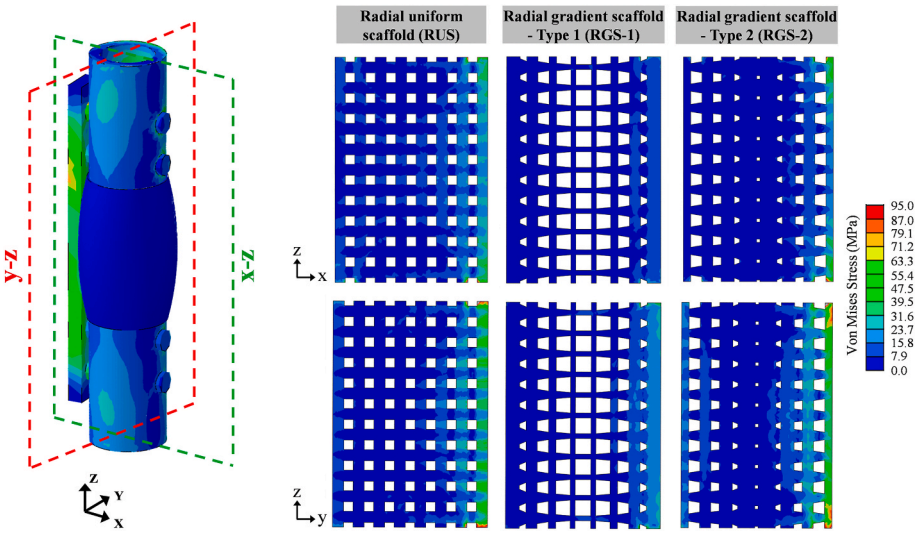



**Fig. 8. Von Mises stress distribution within radial uniform scaffold and radial gradient scaffolds (Type 1 and Type 2) under loading.** The top row shows the stress distribution across the mid-cross-section in the x–z plane, while the bottom row presents the distribution across the y–z plane, demonstrating the influence of scaffold architecture on stress distribution.

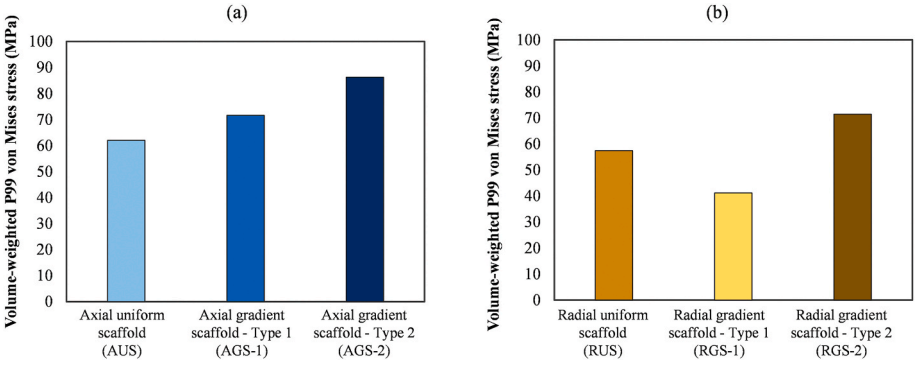



**Fig. 9. Volume-weighted P99 von Mises stress within the scaffold for (a) axial and (b) radial scaffold configurations.** P99 stress was calculated from integration-point stress values using integration-point volume as the weighting factor.

vascularisation was not explicitly modelled despite its critical role in regeneration. Future configuration-matched mechanical testing and animal studies are therefore needed to evaluate these computational predictions and confirm their translational relevance. Future work should also extend the framework to degradable materials, incorporate subject-specific geometries and loading conditions, and couple the model with angiogenesis simulations. In addition, integration with optimisation algorithms, including machine-learning-based approaches (Wu et al., 2024a, 2024b), could enable automated discovery of scaffold designs that balance mechanical and biological outcomes.

## 4. Conclusion

Within the investigated design space, pore-size-gradient orientation and direction influenced the balance between predicted bone regeneration and scaffold stress. Among the axial designs, positioning larger pores at the bone–scaffold interfaces was associated with greater predicted bone occupancy, whereas among the radial designs, increasing peripheral strut density was associated with lower volume-weighted P99 scaffold stress. These findings indicate that functionally graded architectures are not uniformly advantageous; their performance depends on the location and direction of the gradient relative to the intended design objective.

Regenerative and mechanical outcomes were not maximised by the same scaffold configuration. Designs that promoted greater tissue infill did not necessarily produce the most favourable scaffold-stress response, while the configuration with the lowest P99 stress did not substantially improve total bone formation. This trade-off supports scaffold optimisation strategies that consider mechanobiological and structural outcomes jointly.

By applying an established coupled FEA–ABM framework consistently across the six configurations, this study provides a comparative basis for screening opposing axial and radial gradient designs before experimental testing. Future work incorporating degradable materials, vascularisation, subject-specific geometries and loading conditions, manufacturing constraints, and configuration-matched mechanical and in vivo validation will be important for improving the predictive and translational value of the framework.

## CRediT authorship contribution statement

**Ali Entezari:** Writing – review & editing, Writing – original draft, Validation, Software, Methodology, Formal analysis, Conceptualization. **Vahid Badali:** Writing – review & editing, Writing – original draft, Validation, Methodology, Formal analysis, Data curation. **Georg N. Duda:** Writing – review & editing, Validation, Formal analysis, Conceptualization. **Sara Checa:** Writing – review & editing, Writing – original draft, Validation, Methodology, Formal analysis,

Conceptualization.

## Declaration of competing interest

The authors declare that they have no known competing financial interests or personal relationships that could have appeared to influence the work reported in this paper.

## Acknowledgements

Ali Entezari acknowledges the support of the Alexander von Humboldt Foundation through a Humboldt Research Fellowship.

## Appendix A. Supplementary data

Supplementary data to this article can be found online at https://doi.org/10.1016/j.jmbbm.2026.107648.

## Data availability

Data will be made available on request.

## References

Appeddu, P.A., Shur, B.D., 1994. Molecular analysis of cell surface beta-1, 4-galactosyltransferase function during cell migration. Proc. Natl. Acad. Sci. 91 (6), 2095–2099.
Asbai-Ghoudan, R., Nasello, G., Pérez, M.Á., Verbruggen, S.W., Ruiz de Galarreta, S., Rodriguez-Florez, N., 2023. In silico assessment of the bone regeneration potential of complex porous scaffolds. Comput. Biol. Med. 165, 107381.
Badali, V., Checa, S., Zehn, M.M., Marinkovic, D., Mohammadkhah, M., 2024. Computational design and evaluation of the mechanical and electrical behavior of a piezoelectric scaffold: a preclinical study. Front. Bioeng. Biotechnol. 11, 1261108.
Bora, R., Shukla, M., Kumar, A., 2023. Finite element analysis based design of biomimetic functionally graded Ti-6Al-4V alloy scaffolds for human cortical bone applications. Mater. Today Proc. 90, 81–85.
Bose, S., Roy, M., Bandyopadhyay, A., 2012. Recent advances in bone tissue engineering scaffolds. Trends Biotechnol. 30 (10), 546–554.
Brochu, B.M., Sturm, S.R., Kawase De Queiroz Goncalves, J.A., Mirsky, N.A., Sandino, A. I., Panthaki, K.Z., Panthaki, K.Z., Nayak, V.V., Daunert, S., Witek, L., Coelho, P.G., 2024. Advances in bioceramics for bone regeneration: a narrative review. Biomimetics 9 (11).
Chen, Y., Zhou, S., Li, Q., 2011. Microstructure design of biodegradable scaffold and its effect on tissue regeneration. Biomaterials 32 (22), 5003–5014.
Dazzi, C., Eichholz, K.F., Freeman, F.E., Kelly, D.J., Checa, S., 2025. An in silico study reveals how architectural and mechanical cues jointly regulate angiogenesis and bone regeneration in 3D printed scaffolds. Comput. Biol. Med. 195, 110574.
De Witte, T.-M., Fratila-Apachitei, L.E., Zadpoor, A.A., Peppas, N.A., 2018. Bone tissue engineering via growth factor delivery: from scaffolds to complex matrices. Regen. Biomater. 5 (4), 197–211.
Deering, J., Mahmoud, D., Rier, E., Lin, Y., do Nascimento Pereira, A.C., Titotto, S., Fang, Q., Wohl, G.R., Deng, F., Grandfield, K., Elbestawi, M.A., Chen, J., 2023. Osseointegration of functionally graded Ti6Al4V porous implants: histology of the pore network. Biomater. Adv. 155, 213697.
Di Luca, A., Ostrowska, B., Lorenzo-Moldero, I., Lepedda, A., Swieszkowski, W., Van Blitterswijk, C., Moroni, L., 2016. Gradients in pore size enhance the osteogenic differentiation of human mesenchymal stromal cells in three-dimensional scaffolds. Sci. Rep. 6 (1), 22898.
Distefano, F., Epasto, G., Zojaji, M., Ploeg, H.-L., 2025. Mechanical design of a novel functionally graded lattice structure for long bone scaffolds. Design 9 (3), 62.
Dubey, A., Jaiswal, S., Lahiri, D., 2022. Promises of functionally graded material in bone regeneration: current trends, properties, and challenges. ACS Biomater. Sci. Eng. 8 (3), 1001–1027.
Duda, G.N., Eckert-Hübner, K., Sokiranski, R., Kreutner, A., Miller, R., Claes, L., 1997. Analysis of inter-fragmentary movement as a function of musculoskeletal loading conditions in sheep. J. Biomech. 31 (3), 201–210.
Entezari, A., Liu, N.-C., Zhang, Z., Fang, J., Wu, C., Wan, B., Swain, M., Li, Q., 2023. Nondeterministic multiobjective optimization of 3D printed ceramic tissue scaffolds. J. Mech. Behav. Biomed. Mater. 138, 105580.
Entezari, A., Liu, N.C., Roohani, I., Zhang, Z., Chen, J., Sarrafpour, B., Zoellner, H., Behi, M., Zreiqat, H., Li, Q., 2020b. On design for additive manufacturing (DAM) parameter and its effects on biomechanical properties of 3D printed ceramic scaffolds. Mater. Today Commun. 23, 101065.
Entezari, A., Roohani, I., Li, G., Dunstan, C.R., Rognon, P., Li, Q., Jiang, X., Zreiqat, H., 2019. Architectural design of 3D printed scaffolds controls the volume and functionality of newly formed bone. Adv. Healthcare Mater. 8 (1), 1801353.
Entezari, A., Swain, M.V., Gooding, J.J., Roohani, I., Li, Q., 2020a. A modular design strategy to integrate mechanotransduction concepts in scaffold-based bone tissue engineering. Acta Biomater. 118, 100–112.
Entezari, A., Wu, Q., Mirkhalaf, M., Lu, Z., Roohani, I., Li, Q., Dunstan, C.R., Jiang, X., Zreiqat, H., 2024. Unraveling the influence of channel size and shape in 3D printed ceramic scaffolds on osteogenesis. Acta Biomater. 180, 115–127.
Fillingham, Y., Jacobs, J., 2016. Bone grafts and their substitutes. Bone Jt. J. 98-b (1 Suppl. A), 6–9.
Gryko, A., Prochor, P., Sajewicz, E., 2022. Finite element analysis of the influence of porosity and pore geometry on mechanical properties of orthopaedic scaffolds. J. Mech. Behav. Biomed. Mater. 132, 105275.
Guo, H., Li, Q., Zreiqat, H., Entezari, A., 2026. Emerging technologies for personalised oro-maxillofacial bone regeneration: design strategies and fabrication techniques. Biomaterials 326, 123709.
Ho-Shui-Ling, A., Bolander, J., Rustom, L.E., Johnson, A.W., Luyten, F.P., Picart, C., 2018. Bone regeneration strategies: engineered scaffolds, bioactive molecules and stem cells current stage and future perspectives. Biomaterials 180, 143–162.
Hollister, S.J., 2005. Porous scaffold design for tissue engineering. Nat. Mater. 4 (7), 518–524.
Huiskes, R., Driel, W.V., Prendergast, P.J., Søballe, K., 1997. A biomechanical regulatory model for periprosthetic fibrous-tissue differentiation. J. Mater. Sci. Mater. Med. 8 (12), 785–788.
Huo, Y., Lu, Y., Meng, L., Wu, J., Gong, T., Zou, J.a., Bosiakov, S., Cheng, L., 2021. A critical review on the design, manufacturing and assessment of the bone scaffold for large bone defects. Front. Bioeng. Biotechnol. 9, 2021.
Jaber, M., Poh, P.S., Duda, G.N., Checa, S., 2022. PCL strut-like scaffolds appear superior to gyroid in terms of bone regeneration within a long bone large defect: an in silico study. Front. Bioeng. Biotechnol. 10, 995266.
Kong, D., Wang, Q., Huang, J., Zhang, Z., Wang, X., Han, Q., Shi, Y., Ji, R., Li, Y., 2023. Design and manufacturing of biomimetic scaffolds for bone repair inspired by bone trabeculae. Comput. Biol. Med. 165, 107369.
Lacroix, D.a., Prendergast, P., 2002. A mechano-regulation model for tissue differentiation during fracture healing: analysis of gap size and loading. J. Biomech. 35 (9), 1163–1171.
Lee, S.S., Du, X., Kim, I., Ferguson, S.J., 2022. Scaffolds for bone-tissue engineering. Matter 5 (9), 2722–2759.
Liu, Y., Wan, Y., Li, C., Guan, G., Wang, F., Gao, J., Wang, L., 2025. Gradient scaffolds in bone-soft tissue interface engineering: structural characteristics, fabrication techniques, and emerging trends. J. Orthop. Transl. 50, 333–353.
Mukasheva, F., Adilova, L., Dyussenbinov, A., Yernaimanova, B., Abilev, M., Akilbekova, D., 2024. Optimizing scaffold pore size for tissue engineering: insights across various tissue types. Front. Bioeng. Biotechnol. 12, 1444986.
Perier-Metz, C., Cipitria, A., Hutmacher, D.W., Duda, G.N., Checa, S., 2022b. An in silico model predicts the impact of scaffold design in large bone defect regeneration. Acta Biomater. 145, 329–341.
Perier-Metz, C., Duda, G.N., Checa, S., 2020. Mechano-biological computer model of scaffold-supported bone regeneration: effect of bone graft and scaffold structure on large bone defect tissue patterning. Front. Bioeng. Biotechnol. 8, 585799.
Perier-Metz, C., Duda, G.N., Checa, S., 2022a. A mechanobiological computer optimization framework to design scaffolds to enhance bone regeneration. Front. Bioeng. Biotechnol. 10, 980727.
Pobloth, A.-M., Checa, S., Razi, H., Petersen, A., Weaver, J.C., Schmidt-Bleek, K., Windolf, M., Tatai, A.Á., Roth, C.P., Schaser, K.-D., Duda, G.N., Schwabe, P., 2018. Mechanobiologically optimized 3D titanium-mesh scaffolds enhance bone regeneration in critical segmental defects in sheep. Sci. Transl. Med. 10 (423), eaam8828.
Rezapourian, M., Hussainova, I., 2023. Optimal mechanical properties of Hydroxyapatite gradient Voronoi porous scaffolds for bone applications — a numerical study. J. Mech. Behav. Biomed. Mater. 148, 106232.
Roseti, L., Parisi, V., Petretta, M., Cavallo, C., Desando, G., Bartolotti, I., Grigolo, B., 2017. Scaffolds for Bone Tissue Engineering: state of the art and new perspectives. Mater. Sci. Eng. C 78, 1246–1262.
Schulze, F., Lang, A., Schoon, J., Wassilew, G.I., Reichert, J., 2023. Scaffold guided bone regeneration for the treatment of large segmental defects in long bones. Biomedicines 11 (2).
Velasco, M.A., Narváez-Tovar, C.A., Garzón-Alvarado, D.A., 2015. Design, materials, and mechanobiology of biodegradable scaffolds for bone tissue engineering. Biomed Res. Int. 2015, 729076.
Wu, C., Fang, J., Entezari, A., Sun, G., Swain, M.V., Xu, Y., Steven, G.P., Li, Q., 2021. A time-dependent mechanobiology-based topology optimization to enhance bone growth in tissue scaffolds. J. Biomech. 117, 110233.
Wu, C., Wan, B., Entezari, A., Fang, J., Xu, Y., Li, Q., 2024b. Machine learning-based design for additive manufacturing in biomedical engineering. Int. J. Mech. Sci. 266, 108828.
Wu, C., Wan, B., Xu, Y., Al Maruf, D.S.A., Cheng, K., Lewin, W.T., Fang, J., Xin, H., Crook, J.M., Clark, J.R., Steven, G.P., Li, Q., 2024a. Dynamic optimisation for graded tissue scaffolds using machine learning techniques. Comput. Methods Appl. Mech. Eng. 425, 116911.
Xiao, F., Ren, G.-h., Pan, C.-y., Xu, X., Cheng, K.-j., You, J., Liu, Y.-f., 2025. Design and in vitro evaluation of gradient Schwarz Primitive scaffolds with thin-board integration for bone implants. Biomater. Adv. 177, 214412.
Xiong, Y.-Z., Gao, R.-N., Zhang, H., Dong, L.-L., Li, J.-T., Li, X., 2020. Rationally designed functionally graded porous Ti6Al4V scaffolds with high strength and toughness built via selective laser melting for load-bearing orthopedic applications. J. Mech. Behav. Biomed. Mater. 104, 103673.

Xu, C., Liu, Z., Chen, X., Gao, Y., Wang, W., Zhuang, X., Zhang, H., Dong, X., 2024a. Bone tissue engineering scaffold materials: fundamentals, advances, and challenges. Chin. Chem. Lett. 35 (2), 109197.

Xu, Y., Zhang, S., Ding, W., Du, H., Li, M., Li, Z., Chen, M., 2024b. Additively-manufactured gradient porous bio-scaffolds: permeability, cytocompatibility and mechanical properties. Compos. Struct. 336, 118021.

Yan, Liwei, Entezari, Ali, Zhang, Zhongpu, Zhong, Jingxiao, Liang, Jing, Li, Qing, Qi, Jian, 2022. An experimental and numerical study of the microstructural and biomechanical properties of human peripheral nerve endoneurium for the design of tissue scaffolds. Frontiers in Bioengineering and Biotechnology 10, 1029416. https://doi.org/10.3389/fbioe.2022.1029416. https://www.frontiersin.org/articles/10.3389/fbioe.2022.1029416/full. (Accessed 5 December 2022).